Chirality-induced orbital Edelstein effect in an analytically solvable model

Börge Göbel,* Lennart Schimpf, and Ingrid Mertig
Institut für Physik, Martin-Luther-Universität Halle-Wittenberg, D-06099 Halle (Saale), Germany

(Received 7 February 2025; accepted 29 July 2025; published 21 August 2025)

Chirality-induced spin selectivity (CISS), a phenomenon wherein chiral structures selectively determine the spin polarization of electron currents flowing through the material, has garnered significant attention due to its potential applications in areas such as spintronics, enantioseparation, and catalysis. The underlying physical effect is the Edelstein effect that converts charge to angular momentum. Besides a spin contribution, there exists a contribution based on the orbital angular momentum but the precise mechanism for its generation remains yet to be understood. Here, we introduce the minimal model for explaining the phenomenon based on the orbital Edelstein effect. We consider nonlocal intersite contributions to the current-induced orbital angular momentum and reveal the underlying mechanism by analytically calculating the Edelstein susceptibilities in a tight-binding and Boltzmann approach. While the orbital angular momentum is directly generated by the chirality of the crystal, the spin contribution of each spin-split band pair relies on spin-orbit coupling. Using tellurium as an example, we show that the orbital contribution surpasses the spin contribution by orders of magnitude.

DOI: 10.1103/vpjm-ntbh

I. INTRODUCTION

Chirality is a geometric property that affects a wide range of scientific fields, from chemistry and biology to physics and material engineering. A structure is chiral if it is distinguishable from its mirror image; it lacks mirror, inversion, and rotoinversion symmetries [1]. The structural chirality of molecules like the DNA molecule or crystals like tellurium and selenium (cf. Fig. 1) can affect biochemical properties and even couples to physical observables like the angular momentum, which gives rise to intriguing phenomena like electrical magnetochiral anisotropy [2–5] and chirality-induced spin selectivity (CISS) [1,5–14]. The chirality of a structure determines the sign of the spin polarization of electrons moving through it. CISS was first observed in chiral molecules [6]. More recently, this phenomenon has been observed in a broader range of systems, including hybrid organic-inorganic perovskites [7,8] and chiral crystals like tellurium [1,9,15] or $CrNb_3S_6$ [5,10].

Despite extensive experimental observations, the underlying physical mechanisms governing CISS remain a topic of active debate. Some theoretical explanations are based on the charge-to-spin conversion effect named inverse spin-galvanic effect or Edelstein effect (EE) [16,17]: Due to a broken inversion symmetry, the spin polarizations of electrons with opposite wave vectors differ, which leads to the generation of a spin density once an electric field or currents are applied. The EE typically occurs at interfaces where the broken inversion symmetry gives rise to a Rashba-type spin-orbit coupling (SOC) [18–20]. In a chiral material, however, the inversion symmetry is innately broken and a collinear effect can occur where the spins are parallel to the wave vector [1,9,15,21,22] and the theoretically calculated Edelstein susceptibilities indeed depend on the chirality of the structure. However, as was pointed out in Refs. [21,22], they are an order of magnitude smaller than what was measured experimentally in tellurium [15] pointing toward the existence of important additional contributions.

Recently, several phenomena related to angular momentum have been observed and understood based on the orbital degree of freedom. Orbital-polarized currents, generated by the orbital Hall effect [23–38] or the orbital EE [39–51] can lead to the generation or transport of orbital angular momentum when currents or electric fields are applied. It has been shown that the orbital EE is sensitive to the chirality of a system as well [40,41,45,46,49]. We refer to this phenomenon as chirality-induced orbital selectivity (CIOS). When a current flows through a chiral material, an orbital magnetic moment is generated due to a shift of the Fermi surfaces, as visualized in Fig. 2. If the chiral material is interfaced with another material, an orbital current may flow. This material may serve as an electrode, which typically has a considerable spin-orbit coupling, for example, Pt. This leads to the conversion of the orbital current into a spin current. The orbital Edelstein effect may then be detected as CISS and not as CIOS, where the orbital contribution is scaled by the orbital-to-spin conversion efficiency of the electrode. This contribution occurs additionally to any genuine spin contribution to CISS and could therefore account for the discrepancy of theoretically and experimentally determined CISS efficiencies. Therefore, understanding the mechanism behind the orbital Edelstein effect in chiral materials is of crucial importance.

*Contact author: boerge.goebel@physik.uni-halle.de

Published by the American Physical Society under the terms of the Creative Commons Attribution 4.0 International license. Further distribution of this work must maintain attribution to the author(s) and the published article's title, journal citation, and DOI.

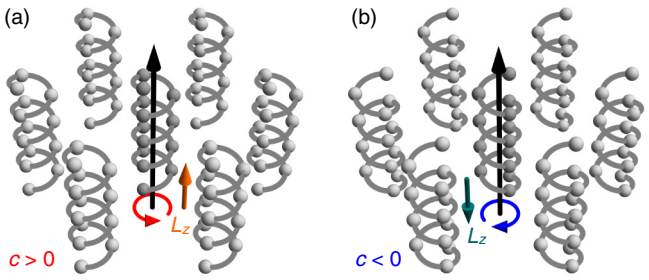


FIG. 1. Chiral helices. (a) Right-handed helix structure characterized by $c > 0$. (b) Left-handed structure characterized by $c < 0$. The black arrow symbolizes the translational motion of electrons along z. It is constrained to a circular motion (red and blue), which generates opposite orbital angular momentum L_z (orange and green) for the two opposite crystal chiralities.

In most theoretical descriptions, orbital angular momentum is calculated via the hybridization of multiple atomic orbitals at the same atom (atomic-center approximation). The efficiency of CIOS is underestimated and can hardly be understood intuitively because the genuine chiral mechanism is not captured: The orbital angular momentum is mostly generated by the circular motion of electrons among *multiple* atoms forming a helix, like in tellurium. This generates an orbital angular momentum that is always along the current direction for one helix chirality and always opposite for the other (cf. arrows in Fig. 1). Even in a semiclassical analysis, we can understand why considering interside hybridization is crucial: Electrons moving along a helix generate a current and orbital angular momentum along the same direction. The orbital-polarized current is independent of the motion direction but changes sign with the chirality of the helix because the angular velocity is proportional to the velocity along the helix and the chirality (cf. Fig. 1). Here, it becomes apparent that the orbital angular momentum is generated due to the circular motion among *multiple* atoms forming the helix and is not introduced by hybridization of orbitals of one atom. Currently, the literature on the orbital Edelstein effect considering such intersite contributions is scarce. References [40,41] use the modern formulation of orbital magnetization [52–57] and even make the analogy to a classical solenoid. However, due to the Haldane-like [58] nature of the model [40,41], requiring multiple independent parameters, the Edelstein susceptibility

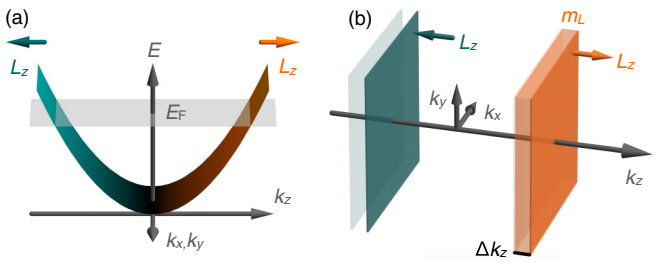


FIG. 2. Orbital Edelstein effect (schematic for $c > 0$). (a) Band structure of free electrons with orbital angular momentum L_z proportional to the group velocity (color). (b) Upon application of an electric field along z, the initial Fermi surfaces (pale) are shifted by Δk_z giving rise to a nonequilibrium orbital magnetic moment $\boldsymbol{m}_L$.

cannot be calculated analytically. Furthermore, the interpretation based on Weyl points in the three-dimensional Brillouin zone dilutes the intuitive mechanism based on the chirality in real space.

In this paper, we introduce the minimal model for understanding the Edelstein effect in chiral materials. The unit cell of the considered helix consists of only three s orbitals and extends periodically along one dimension. We consider the modern formulation of orbital magnetization for the calculation of the orbital angular momentum to account for intersite contributions that are crucial for describing the effect in chiral materials properly. Since we can describe this system analytically, we are able to reveal the chiral mechanism of CIOS and CISS based on an orbital EE that is orders of magnitude larger than the spin EE.

This paper is structured as follows. First, we introduce the model and analytically calculate the band structure, orbital angular momentum, and the orbital Edelstein susceptibility in Sec. II. Afterward, in Sec. III, we discuss the consequences of two important effects present in real materials: dispersion perpendicular to the helix direction and spin-orbit coupling. In Sec. IV, we show that the analytical model can be even further simplified by making use of a constraint between the angular velocity and the velocity along the helix, as in a classical analysis. We discuss our results and conclude in Sec. V.

II. ORBITAL EDELSTEIN EFFECT IN ANALYTICALLY SOLVABLE MODEL

The model consists of the most fundamental chiral structure: a helix consisting of three atoms akin to the structure in tellurium and resembling its space group $P3_121$ (D_3^4 symmetry) or $P3_221$ (D_3^6 symmetry), depending on the chirality [15]. The three basis atoms positioned at $\boldsymbol{r}_1 = (0, 0, 0), \boldsymbol{r}_2 = (a, 0, \frac{1}{3}c), \boldsymbol{r}_3 = (\frac{1}{2}a, \frac{\sqrt{3}}{2}a, \frac{2}{3}c)$ host a single s orbital and give rise to hopping paths along

$$\begin{aligned} \boldsymbol{r}_{12} &= \left(a, 0, \tfrac{1}{3}c\right), \\ \boldsymbol{r}_{23} &= \left(-\tfrac{1}{2}a, \tfrac{\sqrt{3}}{2}a, \tfrac{1}{3}c\right), \\ \boldsymbol{r}_{31} &= \left(-\tfrac{1}{2}a, -\tfrac{\sqrt{3}}{2}a, \tfrac{1}{3}c\right). \end{aligned} \tag{1}$$

The chiral structure is considered periodic along the z direction with a period of c. The sign of c controls the chirality of the helix: right-handed for $c > 0$ and left-handed for $c < 0$ (cf. Fig. 1). We also consider periodicity in the xy plane but for simplicity the helices are not coupled by hoppings. This allows us to describe the chiral structure in an effectively one-dimensional Brillouin zone with k_z the only wave vector component that exhibits dispersion. The x and y coordinates of the atoms are important to account for the chirality and for the definition of the orbital angular momentum.

A. Hamiltonian and band structure

The tight-binding Hamiltonian requires only a single parameter (nearest-neighbor hopping amplitude t) to capture the chiral mechanism of CIOS:

$$H(\boldsymbol{k}) = -t \begin{pmatrix} 0 & e^{i\boldsymbol{k}\cdot\boldsymbol{r}_{12}} & e^{-i\boldsymbol{k}\cdot\boldsymbol{r}_{31}} \\ e^{-i\boldsymbol{k}\cdot\boldsymbol{r}_{12}} & 0 & e^{i\boldsymbol{k}\cdot\boldsymbol{r}_{23}} \\ e^{i\boldsymbol{k}\cdot\boldsymbol{r}_{31}} & e^{-i\boldsymbol{k}\cdot\boldsymbol{r}_{23}} & 0 \end{pmatrix}. \tag{2}$$

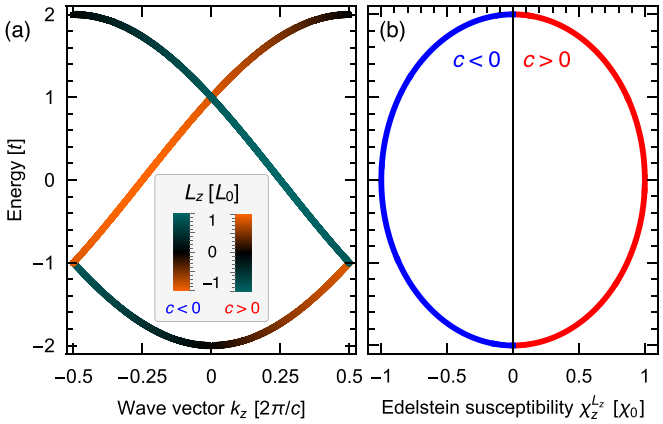


FIG. 3. Chirality-induced orbital selectivity in a chiral system without spin-orbit coupling. (a) Band structure for which the color encodes the orbital angular momentum L_z in units of $L_0 = \frac{1}{\sqrt{3}}\frac{m_e}{g_L\hbar}a^2t$. (b) Edelstein susceptibility $\chi_z^{L_z}$ in units of $\chi_0 = \frac{e^2}{2\pi\sqrt{3}\hbar^2}\tau\,|t|ca^2$. The red curve shows the result for the right-handed system ($c > 0$) and the blue curve for the left-handed system ($c < 0$).

Due to the lack of dispersion along k_x and k_y, the band structure along $k \equiv k_z$ reads

$$E_1(k) = -2t\cos\left(k\frac{c}{3}\right), \quad E_{2,3}(k) = E_1\left(k \pm \frac{2\pi}{c}\right).$$

This band structure [Fig. 3(a)] is equivalent to the single band $-2t\cos(k\frac{c}{3})$ characterizing a one-dimensional chain of atoms with lattice constant $c/3$ along z, which has been back-folded into the smaller Brillouin zone accounting for the three atoms in the unit cell. Note that the band structure can be very easily calculated by diagonalizing the Hamiltonian for $k_x = k_y = 0$. The eigenvectors $|n\rangle$ along k_z are constant and read

$$|1\rangle = \frac{1}{\sqrt{3}}\begin{pmatrix}1\\1\\1\end{pmatrix}, \quad |2,3\rangle = \frac{1}{\sqrt{3}}\begin{pmatrix}1\\-1/2 \pm i\sqrt{3}/2\\-1/2 \mp i\sqrt{3}/2\end{pmatrix}.$$

B. Orbital angular momentum

We calculate the z component of the orbital angular momentum of the nth band based on the modern formulation of orbital magnetization [52–57]:

$$L_{n,z}(\boldsymbol{k}) = i\frac{m_e}{g_L\hbar}\sum_{m\neq n}\frac{1}{E_m(\boldsymbol{k}) - E_n(\boldsymbol{k})} \times [\langle n|\partial H/\partial k_x|m\rangle\langle m|\partial H/\partial k_y|n\rangle - (n \leftrightarrow m)]. \tag{3}$$

The derivatives of the Hamiltonian $\partial H/\partial k_x$, $\partial H/\partial k_y$ account for the chirality of the system. This results in a chirality-dependent orbital angular momentum (opposite for $c > 0$ versus $c < 0$)

$$L_{1,z}(k) = \frac{1}{\sqrt{3}}\frac{m_e}{g_L\hbar}a^2t\,\sin\left(k\frac{c}{3}\right), \tag{4}$$

$$L_{2/3,z}(k) = L_{1,z}\left(k \pm \frac{2\pi}{c}\right) \tag{5}$$

that is proportional to the group velocity $v_{n,z}(k) = \frac{1}{\hbar}\frac{\partial E_n}{\partial k_z}$.

C. Orbital Edelstein effect

The fact that the orbital angular momentum is antisymmetric with k, while the band structure is symmetric [cf. also Fig. 3(a)], gives rise to an orbital Edelstein effect, as visualized in Fig. 2. The collinear orbital Edelstein susceptibility $\chi_z^{L_z}$ relates the applied electric field $\boldsymbol{E} = E_z\boldsymbol{e}_z$ and the generated nonequilibrium orbital magnetic moment per unit cell $m_{L_z}^{\mathrm{uc}}$ via $m_{L_z}^{\mathrm{uc}} = \chi_z^{L_z}E_z$. We can calculate $\chi_z^{L_z}$ easily using the Boltzmann transport theory when we assume a constant relaxation time τ:

$$\chi_z^{L_z}(E) = \frac{e^2 g_L}{2m_e}\tau\sum_{n,\boldsymbol{k}} v_{n,z}(k)\cdot L_{n,z}(k)\cdot\delta(E_n(k) - E). \tag{6}$$

This results in

$$\chi_z^{L_z}(E) = \frac{e^2}{2\pi\sqrt{3}\hbar^2}\tau\,|t|ca^2\sqrt{1 - \left(\frac{E}{2t}\right)^2}. \tag{7}$$

The result is proportional to $L_{n,z}^{(k>0)}(E) - L_{n,z}^{(k<0)}(E)$. Therefore, we can easily understand the energy dependence as presented in Fig. 3(b). $\chi_z^{L_z}$ is zero at the band edges due to the zero velocity and is largest in the middle of the band width where the velocity and therefore L_z are largest as well. The orbital Edelstein susceptibility changes sign once the chirality is reversed, due to the linear c dependence [59].

So far, we wanted to make the discussion as general as possible. Now we consider the case of tellurium's s bands that exhibit an almost perfect resemblance of the band structure we have calculated. We use $a = 2.133$ Å, $t = 1.249$ eV [60], and $g_L = 1$, which gives a maximum value for the orbital angular momentum $L_0 = 0.43\,\hbar$. For the orbital Edelstein susceptibility, we additionally use $c = \pm 6.018$ Å and assume a relaxation time $\tau = 1$ ps, which results in an extremum of $\chi_0 = \pm 125.0 \times 10^{-9}\,\mu_B$ m/V. Note that the magnitude of this signal scales with the relaxation time which is a parameter in our calculations. The sign depends on the crystal chirality, which means the system exhibits an extremely strong yet purely geometrical orbital Edelstein effect. In our model $\chi_z^{S_z} = 0$, because spin is not yet considered.

III. ADDITIONAL EFFECTS PRESENT IN REAL MATERIALS

After having established the main result of the paper, we test its validity by comparison with a three-dimensional model (cf. Sec. III A). Afterward, we present how including SOC influences the orbital Edelstein effect and may cause a spin Edelstein effect as well; two effects relying on distinct mechanisms (cf. Sec. III B).

A. Hopping between the helices

We note that we have restricted our model to quasi-one dimension, so that we can solve it analytically. In reality, the individual helices are coupled by van der Waals interactions, and dispersion along k_x and k_y emerges. However, especially near the center of the energy range, the Fermi surfaces are sheets that extend throughout the whole k_xk_y plane of the three-dimensional Brillouin zone, similar to the schematics

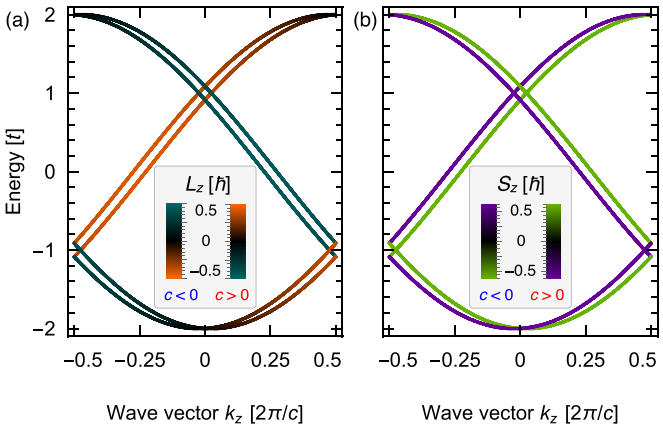


FIG. 4. Band structure of a chiral helix with spin-orbit coupling. (a) The color encodes the orbital angular momentum L_z. (b) The color encodes the spin S_z. Parameters correspond to tellurium with exaggerated spin-orbit coupling $\lambda = 0.05t$.

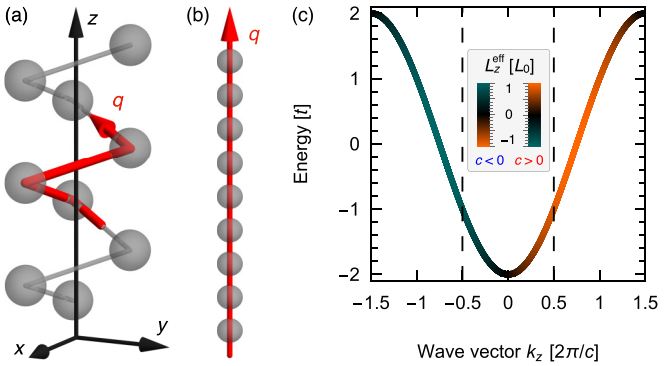


FIG. 5. Effective one-band model. (a) Helix structure for $c > 0$ with generalized coordinate q (red). (b) Structure along this new effective coordinate. (c) Band structure with effective orbital angular momentum (color). The dashed line indicates the smaller Brillouin zone corresponding to a chain with three atoms in the unit cell.

shown in Fig. 2(b). In Appendix A, we show that the full three-dimensional system is described well by the quasi-one-dimensional analytical model.

B. Influence of spin-orbit coupling

The following discussion is again for the one-dimensional model discussed in Sec. II. To include the effect of SOC, first, we make the Hamiltonian spin-dependent. Without SOC, all bands are now doubly degenerate but the orbital angular momentum always has the same value for the two uncoupled spin subsystems. Therefore, the orbital Edelstein susceptibility $\chi_z^{L_z}(E)$ is simply increased by a factor of 2 to a maximum of $250.0 \times 10^{-9}\,\mu_B\,\mathrm{m/V}$. The spin Edelstein susceptibility $\chi_z^{S_z}(E) = 0$ due to Kramer's degeneracy.

SOC is included via a spin- and chirality-dependent hopping term along the helix direction. We introduce the term in Appendix B and explain that it corresponds to a reduced version of the Kane-Mele SOC term [61]. The resulting band structure exhibits spin-split bands in which the energy is slightly shifted along the $\pm k_z$ direction. Likewise, the orbital angular momentum is also only slightly affected by this shift along $\pm k_z$ [cf. Fig. 4(a)]. The analytical calculations are presented in Appendix B.

For the orbital Edelstein susceptibility, we get the same energy-dependent curve as without SOC but with a rescaled bandwidth $\tilde{t}_\lambda = t\sqrt{1 + (\lambda/t)^2}$, where λ quantifies the SOC strength (cf. Appendix B). Even if the SOC were 5% of the hopping amplitude $\lambda = 0.05t$, the maximum of the orbital Edelstein susceptibility changes by only 0.125%. This highlights that the orbital Edelstein effect is not governed by SOC but purely by the chiral structure of the helices. The contributions of the inner and outer bands to the spin Edelstein susceptibility cancel, $\chi_z^{S_z} = 0$. In Appendix C, we analyze that once a spin EE emerges, e.g., by considering a k-dependent relaxation time, it is proportional to spin-orbit coupling and orders of magnitude smaller than the orbital EE.

IV. EFFECTIVE SINGLE-BAND DESCRIPTION

Lastly, we want to compare the quantum-mechanical results with a classical description using constraints. If an electron moves along the helix, it carries out a net motion along z superimposed by a periodic motion along the edges of a triangle in the xy plane. The latter generates an orbital angular momentum $L_z = m_e \frac{a}{2\sqrt{3}} v_{xy}$ with respect to the center of this triangle. The geometry introduces a constraint of the periodic and translational motion: The in-plane velocity along the sides of the triangle v_{xy} is proportional to the velocity along the periodic direction v_z, so $v_{xy} = v_z \cdot 3a/c$. This means that the orbital angular momentum and the velocity along z are proportional to each other $L_z^{\text{classical}} = m_e \frac{\sqrt{3}a^2}{2c} v_z$, which is a signature of the system's chirality.

If we carry over this result to the quantum-mechanical tight-binding model, we can effectively describe the system by a single band (or band pair when spin is considered). The initial system [Fig. 5(a)] with a generalized coordinate q is mapped to a one-dimensional chain along z with lattice constant $c/3$ [Fig. 5(b)], and the Brillouin zone is now three times as large along k_z as before. This mapping is possible because the local environment of all three basis atoms in the helix is equivalent: We can go from one atom to another by rotation and translation.

The one-dimensional chain by itself is not chiral anymore and motion along the chain would not give rise to an orbital angular momentum. However, we can account for the periodic in-plane motion by introducing an effective orbital angular momentum operator L_z^{eff}. It is derived by replacing the Hamilton function $\mathcal{H}$ with the Hamilton operator H^{eff} for the calculation of the velocity along the helix direction $v_z = \frac{\partial \mathcal{H}}{\partial p_z} \to v_z = \frac{1}{\hbar}\frac{\partial H^{\text{eff}}}{\partial k_z}$ leading to

$$L_z^{\text{eff}} = m_e \frac{\sqrt{3}a^2}{2c\hbar} \frac{\partial H^{\text{eff}}}{\partial k_z}. \tag{8}$$

Together with this operator, the effective Hamiltonian

$$H^{\text{eff}}(k_z) = -2t\cos(k_z c/3)\sigma_0 - 2\lambda \sin(k_z c/3)\sigma_z \tag{9}$$

gives rise to the exact same Edelstein susceptibilities $\chi_z^{L_z}(E)$ and $\chi_z^{S_z}(E)$ as the full model considered before, in agreement

with the Ehrenfest theorem. This is because $E(k_z)$, $L_z(k_z)$, and $S_z(k_z)$ are the same as before only that the system is now described in a larger Brillouin zone [Fig. 5(c)]. This effective two-band description (or one-band description without spin) shows that a semiclassical explanation of CIOS is applicable and allows us to understand even easier why the orbital EE is much larger than the spin EE.

Note, that this analogy is only truly valid when the helices are not coupled by hopping terms so that $L_z \propto v_z$. However, as we have shown in Appendix A, the analytical results even agree well with the numerical calculations based on a full three-dimensional description.

V. CONCLUSION

We have shown that the orbital Edelstein effect in a helix is generated by nonlocal intersite contributions and is not generated by the hybridization of quantum-mechanical orbitals at a single atom. This new mechanism is fundamentally different from previously proposed mechanisms because it originates purely from the chirality of the system and can be understood even classically without the need for spin-orbit coupling.

We have analytically shown that the current-induced selectivities of spin and orbital angular momentum in chiral materials follow fundamentally different mechanisms. The orbital contributions from bands with opposite spin directions add up and the effect occurs even without SOC. Within our model, the spin EE of both bands (almost) cancels and scales with SOC making it a less efficient mechanism. However, we note that additional contributions to the spin EE can emerge when terms are added that we have not considered in our minimal model. For example, the model calculations of Ref. [9] consider not only hopping terms in the plane between the helices but also an in-plane spin-momentum locking. To test the applicability of our model and the validity of the conclusions, it will be crucial to distinguish the spin and orbital contributions to the measured Edelstein effect in the future, for example, in tellurium.

The generated Edelstein effect is also very different from the conventional Rashba-Edelstein effect, typically generated by the Rashba interaction at interfaces, because (1) the generated current-induced orbital magnetic moment is oriented along the current direction (versus perpendicular for Rashba), (2) it is a nonlocal effect that occurs all throughout the helix (versus localized at the interface for Rashba), (3) it is caused purely by the chirality of the helix and not by spin-orbit coupling (versus by spin-orbit coupling and a broken inversion symmetry for Rashba), and (4) it has its origin in the real-space chirality (versus relying on spin-momentum locking in reciprocal space for Rashba).

Our findings are significant for intuitively understanding the mechanism behind the orbital Edelstein effect in chiral materials but also motivate more detailed research to find ideal chiral materials that can be used for applications. A large orbital Edelstein effect can be used to generate large torques that are important for spin-orbitronic devices. For example, in Ref. [62] we have shown that in chiral carbon nanotubes the mechanism for the orbital Edelstein effect is in principle the same as we have presented here. However, there exist many different chiral hopping paths along a chiral nanotube. Therefore, a direct relation to the semiclassical explanation of the effect is not always possible and the influence of the complicated subband structure has to be considered as well for most energies.

Recently, several options for the detection of orbital magnetic moments and orbital currents have been demonstrated [63]: (1) by measuring orbital torques as in Ref. [64], (2) via magneto-optical Kerr effect measurements as in Refs. [34,35], (3) by detecting charge currents via inverse orbital effects as in Ref. [47], and (4) via the Hanle magnetoresistance as in Ref. [65]. We would like to highlight here especially Ref. [47] in which the inverse orbital Edelstein effect has been measured at a $LaAlO_3/SrTiO_3$ interface. Furthermore, as explained in the introduction, if a spin signal is measured (as for detecting CISS), the current-induced orbital moment will lead to an orbital current that will be converted into a spin current upon passing through the detecting electrode. So, CIOS might effectively be detected as CISS in addition to any genuine CISS signal. Therefore, our work helps filling the gap between the experimentally observed signals and the too small Edelstein signals that were calculated before based only on the spin EE or the orbital EE effect in the atomic-center approximation.

ACKNOWLEDGMENTS

This work was supported by the EIC Pathfinder OPEN Grant No. 101129641 "Orbital Engineering for Innovative Electronics." B.G. and L.S. performed calculations. B.G. did the analytical derivations, prepared the figures, and planned and supervised the project. All authors discussed the results. B.G. wrote the manuscript with significant inputs from all authors. I.M. provided the funding.

DATA AVAILABILITY

The data that support the findings of this article are openly available [66].

APPENDIX A: COMPARISON WITH A THREE-DIMENSIONAL MODEL

In the main text of this paper, the helices are not coupled by hoppings which leads to flat bands along k_x and k_y.

1. In-plane hopping between helices

First, we couple the helices by considering hoppings in the xy plane, as presented in Fig. 6(a). The band structure [Fig. 6(b)] exhibits dispersion along the k_x and k_y directions and the model is not effectively one-dimensional anymore.

Still, the energy-dependent orbital Edelstein susceptibility [Fig. 6(c)] is described by the one-dimensional model (dashed lines) exceptionally well. This is especially the case in the energy range $-1.7t \lesssim E_F \lesssim 1.4t$ where the Fermi surfaces are nearly planar sheets [Fig. 6(f)] that extend throughout the entire k_xk_y plane as in Fig. 2(b). Near the band edges, the Edelstein susceptibility deviates from the analytical result derived from the one-dimensional model because the dispersion along k_x and k_y causes the Fermi surfaces to turn into deformed spheres [Figs. 6(d) and 6(h)] whose surface area is finite and

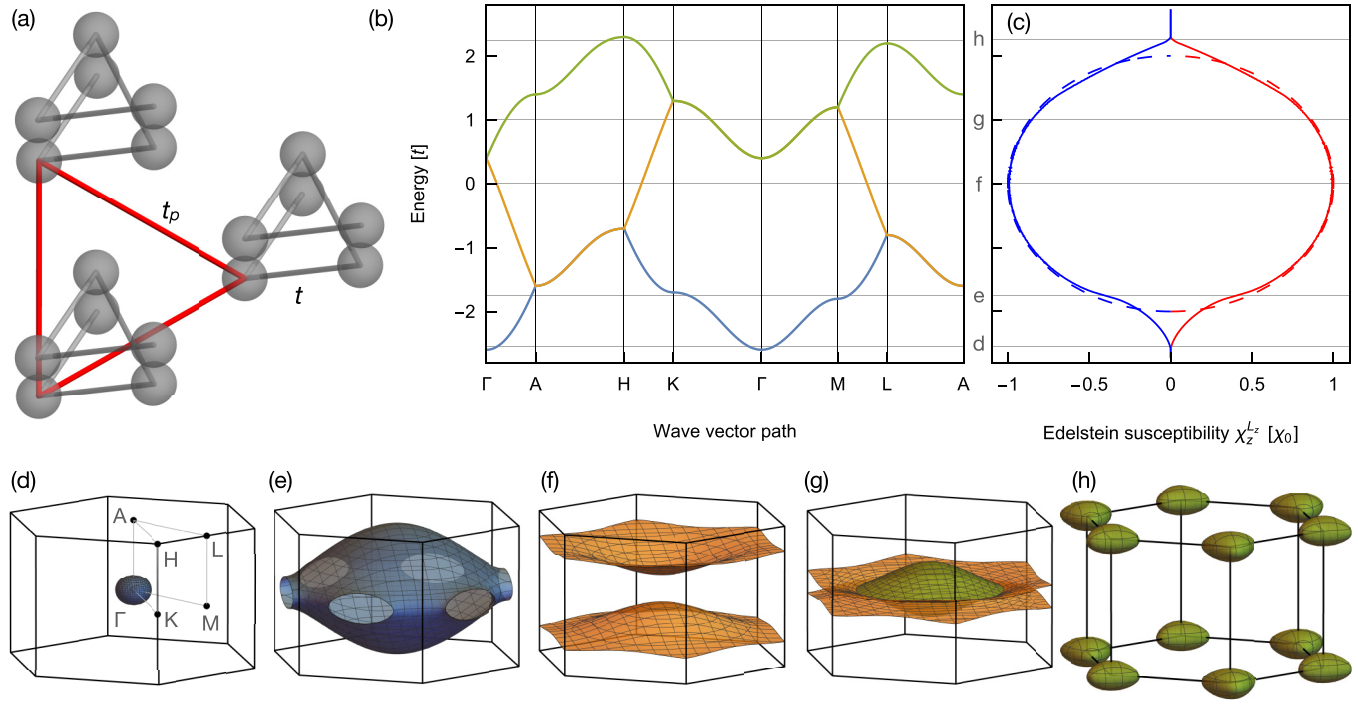


FIG. 6. Chirality-induced orbital selectivity in a three-dimensional model. (a) Example of additional hopping paths considered in this calculation (red). (b) Band structure for $t_p = 0.1t$. (c) Orbital Edelstein susceptibility in units of $\chi_0 = \frac{e^2}{2\pi\sqrt{3}\hbar^2}\tau\,|t|ca^2$ that has been calculated numerically for positive (red) and negative (blue) chirality. The dashed line corresponds to the analytical results derived from the one-dimensional model ($t_p = 0$), as presented in Fig. 3(b). (d)–(h) Fermi surfaces at energies $-2.55t$, $-1.75t$, $0t$, $1t$, and $2.25t$, respectively.

changes considerably with energy. This effect is not captured by the one-dimensional model.

2. Chiral second-nearest-neighbor hopping

For the lattice parameters $a = 2.133$ Å, $b = 4.461$ Å (distance between the helices), and $c = 6.018$ Å of tellurium, the second-nearest-neighbor hoppings are not the hoppings in the xy plane but the ones indicated in Fig. 7(a). This gives rise to a richer energy dependence of the Edelstein susceptibility that exhibits minima and maxima [Fig. 7(c)] and to Fermi surfaces that consist of multiple different shapes [Figs. 7(e) and 7(g)].

Still, the Edelstein susceptibility can be fitted by the results derived from the analytical model in the main text [dashed lines in Fig. 7(c)]. This works especially well near the center of the energy range where the Fermi surfaces are still nearly planar sheets [Fig. 7(f)] that extend throughout the whole k_xk_y plane as in Fig. 2(b).

The newly considered hoppings with amplitude t_2 are chiral and couple the dispersion along k_z with the dispersion along the k_x and k_y directions. Due to the interplay with the other chiral hoppings with amplitude t, that have been considered before, the velocity along z and the orbital angular momentum L_z are not always proportional to each other and can even have opposite signs. This gives rise to the minima and maxima in the Edelstein susceptibility [Fig. 7(c)] that can be fitted with distinct parameters, respectively.

APPENDIX B: INFLUENCE OF SPIN-ORBIT COUPLING

SOC is included akin to a reduced Kane-Mele term [61] by using a spin-dependent hopping along the helix. The term can be written in second quantization:

$$i\lambda \sum_{\langle i,j\rangle} \nu_{ij} c_i^\dagger \sigma_z c_j. \tag{B1}$$

Here, $c_i^\dagger$ and c_j are the creation and annihilation operators at sites i and j, respectively. $\nu_{ij} = \pm 1$ accounts for the hopping path along the helix: $+1$ for a counter-clockwise rotation and -1 for a clockwise rotation, so $+\mathrm{sign}(c)$ for hopping along $+z$ and $-\mathrm{sign}(c)$ for hopping along $-z$. In our 6×6 matrix, this leads to a rescaling of the hopping: $t \to t_{\pm,c} = (t \pm i\lambda)$ where the sign is determined by the spin orientation and the chirality of the helix $\mathrm{sign}(c)$.

The resulting band structure [Figs. 4(a) and 4(b)] is

$$E_1^{\uparrow\downarrow}(k) = -2t\cos\left(k\frac{c}{3}\right) \mp 2\lambda \sin\left(k\frac{c}{3}\right),$$
$$E_{2/3}^{\uparrow\downarrow}(k) = E_1^{\uparrow\downarrow}\left(k \pm \frac{2\pi}{c}\right). \tag{B2}$$

SOC leads to a shift of the bands along the $\pm k_z$ direction. Note the sign change of the SOC term for $c > 0$ and $c < 0$: The sine function comes from adding the two hopping terms along $\pm c\boldsymbol{e}_z$ where the upward hopping path along the helix is rotating oppositely to the downward hopping path: $i[\exp(ick_z) - \exp(-ick_z)]$. Furthermore, it depends on the spin orientation. Close to the Γ point, the SOC-induced term is $\mp 2\lambda k_z c/3$, a term that has been derived in Ref. [67] as well.

The Hamiltonian is separated into spin-up and spin-down blocks meaning that all bands are $\pm 100\%$ spin polarized, $S_{n,z}^{\uparrow\downarrow}(k) = \pm\frac{\hbar}{2}$ [color in Fig. 4(b)]. This makes the system under consideration similar to a Dresselhaus

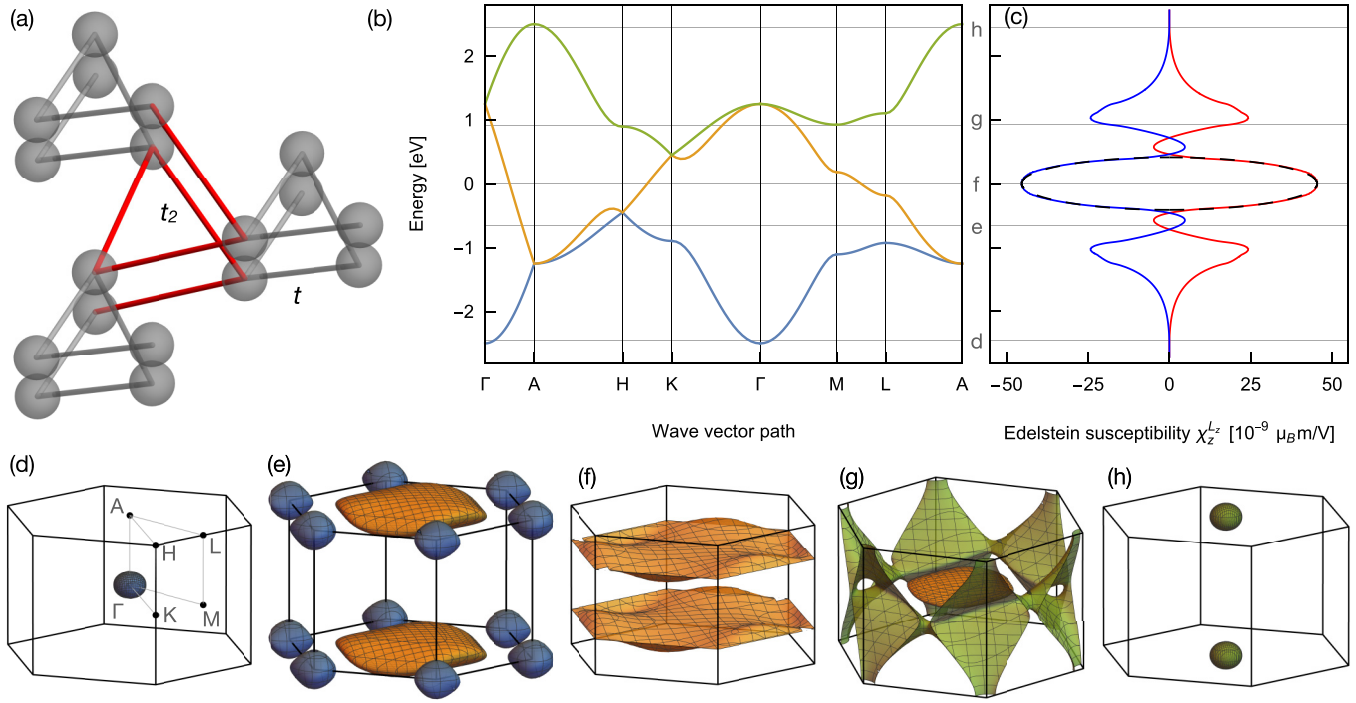


FIG. 7. Chirality-induced orbital selectivity in a three-dimensional model. (a) Example of additional hopping paths considered in this calculation (red). (b) Band structure of the s bands of tellurium. (c) Orbital Edelstein susceptibility that has been calculated numerically for positive (red) and negative (blue) chirality. The dashed line shows a fit using the analytically derived result based on the one-dimensional model. (d)–(h) Fermi surfaces at energies −2.45, −0.65, 0, 0.92, and 2.45 eV, respectively. The hopping amplitudes are $t = 0.714\,87$ eV and $t_2 = 0.267\,566$ eV, fitting the band structure of Ref. [60].

system [68], where the structural chirality breaks the inversion symmetry, but in one dimension. The spin is (anti)parallel to $\boldsymbol{k}$; a feature well known from the Fermi surface of tellurium so the expected spin Edelstein effect is collinear [1,9,15,21,22] meaning that electric field and generated magnetic moment are collinear.

In contrast, the orbital angular momenta of the two bands of each spin-split band pair are almost the same [Fig. 4(a)]. They are affected in a similar way as the band structure:

$$L_{1,z}^{\uparrow\downarrow}(k) = \frac{1}{\sqrt{3}}\frac{m_e}{g_L\hbar}a^2\left[t\sin\left(k\frac{c}{3}\right) \mp \lambda\cos\left(k\frac{c}{3}\right)\right],$$
$$L_{2/3,z}^{\uparrow\downarrow}(k) = L_{1,z}^{\uparrow\downarrow}\left(k \pm \frac{2\pi}{c}\right), \tag{B3}$$

and so the orbital Edelstein susceptibility is merely rescaled due to the new bandwidth $\tilde{t}_\lambda = t\sqrt{1+(\lambda/t)^2}$:

$$\chi_z^{L_z}(E) = \frac{e^2}{\pi\sqrt{3}\,\hbar^2}\tau c a^2\,|\tilde{t}_\lambda|\sqrt{1-\left(\frac{E}{2\tilde{t}_\lambda}\right)^2}. \tag{B4}$$

Note that the SOC term [Eq. (B1)] contains only σ_z, while a strict SOC term according to the Kane-Mele model [61] would include also σ_x and σ_y. The preferred spin orientation is not anymore perfectly aligned with the helix direction but slightly tilted along the hopping path for each nearest-neighbor hopping. However, since each Bloch state is homogeneously distributed over all three atoms in the unit cell in our model, this tilting cancels after three nearest-neighbor hoppings within a unit cell. The spin expectation value does not have an in-plane component but is slightly reduced from $\pm\hbar/2$. We disregard this small quantitative effect by neglecting the σ_x and σ_y terms, similar to what has been done in Ref. [67] because then we are still able to solve the system analytically and because it does not qualitatively affect our results.

APPENDIX C: EDELSTEIN EFFECT UNDER k-DEPENDENT RELAXATION TIME

To distinguish the here predicted CIOS from the genuine CISS, we calculate the spin Edelstein susceptibility:

$$\chi_z^{S_z}(E) = \frac{e^2 g_S}{2m_e}\tau\sum_{n,\boldsymbol{k}} v_{n,z}(k)\cdot S_{n,z}(k)\cdot\delta(E_n(k)-E). \tag{C1}$$

In the considered constant relaxation time approximation, SOC does not lead to a spin Edelstein effect because the contributions of the spin-up and spin-down bands cancel, as has been explained in the main text and in Appendix B.

To generate such an effect, we have several options but all rely on an interplay of multiple effects and therefore generate a rather small signal compared to the orbital Edelstein effect. An example is to consider a conventional Rashba term in the xy plane additionally to the chiral SOC term along z, similar to what has been done in Ref. [9]. Here, we want to present another possibility and consider a k-dependent relaxation time.

Assuming a symmetric relaxation time in k and accounting for periodicity, it is $\tau_k = \tau_0[1+\xi\cos(kc/3)]$.

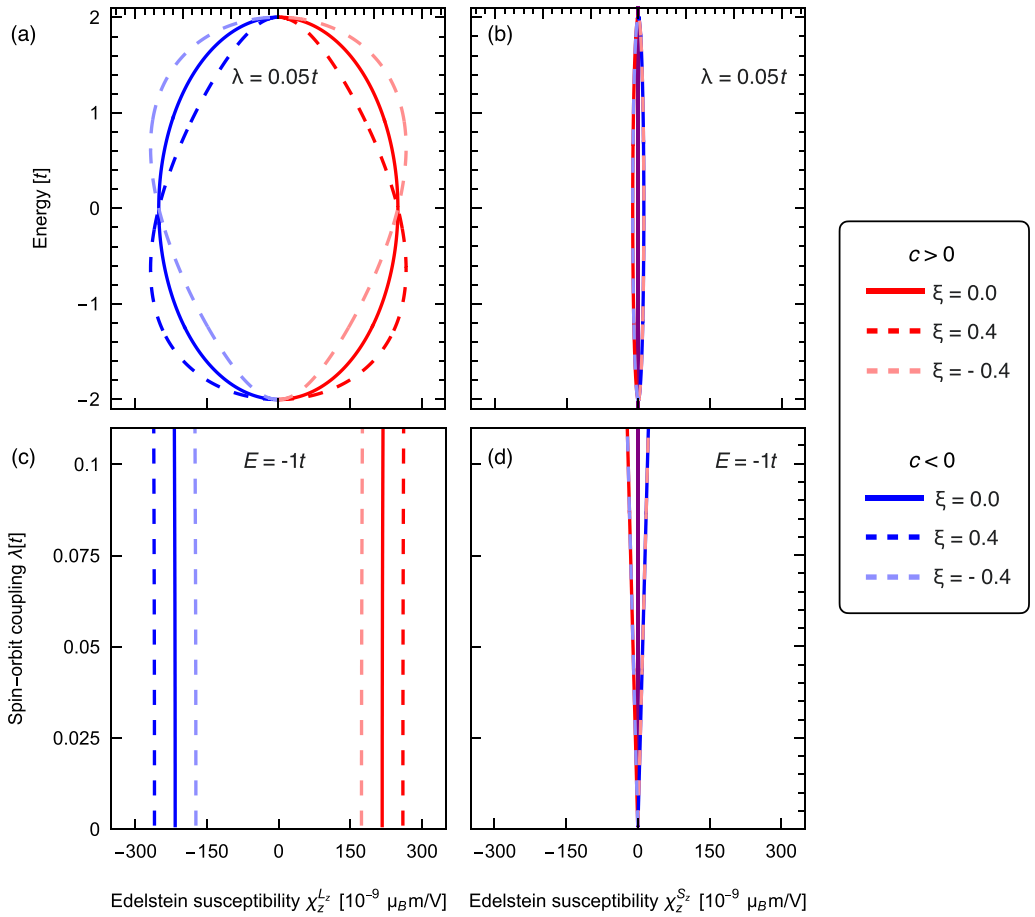


FIG. 8. Parameter scaling of the Edelstein susceptibilities. (a) Orbital Edelstein susceptibility $\chi_z^{L_z}$ and (b) spin Edelstein susceptibility $\chi_z^{S_z}$ for a fixed spin-orbit coupling $\lambda = 0.05t$ and different values for the k-dependent relaxation time ξ (see legend). The energy-dependent curves are opposite for positive (red) and negative (blue) chirality. (c), (d) Edelstein susceptibilities as a function of spin-orbit coupling λ for a fixed location of the Fermi energy $E = -1t$. Parameters are chosen as in Fig. 4 and correspond to tellurium.

The resulting Edelstein susceptibilities are

$$\chi_z^{S_z}(E) = -\frac{e^2 g_S}{2m\pi}\tau\xi c\,\frac{\lambda}{|\tilde{t}_\lambda|}\sqrt{1-\left(\frac{E}{2\tilde{t}_\lambda}\right)^2},$$
$$\chi_z^{L_z}(E) = \frac{e^2}{\pi\sqrt{3}\,\hbar^2}\tau c a^2\left(|\tilde{t}_\lambda| - \frac{1}{2}\frac{t}{|\tilde{t}_\lambda|}E\xi\right)\sqrt{1-\left(\frac{E}{2\tilde{t}_\lambda}\right)^2}. \tag{C2}$$

Note that now there is a finite $\chi_z^{S_z}$ and its sign depends on the chirality, the sign of ξ, and the sign of the SOC. Still, the orbital contribution dominates and is only slightly affected by SOC. These quantities and their parameter scaling are shown in Fig. 8.

[1] T. Furukawa, Y. Watanabe, N. Ogasawara, K. Kobayashi, and T. Itou, Current-induced magnetization caused by crystal chirality in nonmagnetic elemental tellurium, Phys. Rev. Res. **3**, 023111 (2021).
[2] G. Rikken, J. Fölling, and P. Wyder, Electrical magnetochiral anisotropy, Phys. Rev. Lett. **87**, 236602 (2001).
[3] F. Pop, P. Auban-Senzier, E. Canadell, G. L. Rikken, and N. Avarvari, Electrical magnetochiral anisotropy in a bulk chiral molecular conductor, Nat. Commun. **5**, 3757 (2014).
[4] R. Aoki, Y. Kousaka, and Y. Togawa, Anomalous nonreciprocal electrical transport on chiral magnetic order, Phys. Rev. Lett. **122**, 057206 (2019).
[5] A. Inui, R. Aoki, Y. Nishiue, K. Shiota, Y. Kousaka, H. Shishido, D. Hirobe, M. Suda, J.-I. Ohe, J.-I. Kishine *et al.*, Chirality-induced spin-polarized state of a chiral crystal $CrNb_3S_6$, Phys. Rev. Lett. **124**, 166602 (2020).
[6] K. Ray, S. Ananthavel, D. Waldeck, and R. Naaman, Asymmetric scattering of polarized electrons by organized organic films of chiral molecules, Science **283**, 814 (1999).

[7] H. Lu, J. Wang, C. Xiao, X. Pan, X. Chen, R. Brunecky, J. J. Berry, K. Zhu, M. C. Beard, and Z. V. Vardeny, Spin-dependent charge transport through 2D chiral hybrid lead-iodide perovskites, Sci. Adv. **5**, eaay0571 (2019).

[8] Z. Huang, B. P. Bloom, X. Ni, Z. N. Georgieva, M. Marciesky, E. Vetter, F. Liu, D. H. Waldeck, and D. Sun, Magneto-optical detection of photoinduced magnetism via chirality-induced spin selectivity in 2D chiral hybrid organic–inorganic perovskites, ACS Nano **14**, 10370 (2020).

[9] F. Calavalle, M. Suárez-Rodríguez, B. Martín-García, A. Johansson, D. C. Vaz, H. Yang, I. V. Maznichenko, S. Ostanin, A. Mateo-Alonso, A. Chuvilin *et al.*, Gate-tuneable and chirality-dependent charge-to-spin conversion in tellurium nanowires, Nat. Mater. **21**, 526 (2022).

[10] Y. Nabei, D. Hirobe, Y. Shimamoto, K. Shiota, A. Inui, Y. Kousaka, Y. Togawa, and H. M. Yamamoto, Current-induced bulk magnetization of a chiral crystal $CrNb_3S_6$, Appl. Phys. Lett. **117**, 052408 (2020).

[11] S. Dalum and P. Hedegård, Theory of chiral induced spin selectivity, Nano Lett. **19**, 5253 (2019).

[12] M. Geyer, R. Gutierrez, and G. Cuniberti, Effective Hamiltonian model for helically constrained quantum systems within adiabatic perturbation theory: Application to the chirality-induced spin selectivity (CISS) effect, J. Chem. Phys. **152**, 214105 (2020).

[13] S.-W. Cheong and X. Xu, Magnetic chirality, npj Quantum Mater. **7**, 40 (2022).

[14] S. Naskar, V. Mujica, and C. Herrmann, Chiral-induced spin selectivity and non-equilibrium spin accumulation in molecules and interfaces: A first-principles study, J. Phys. Chem. Lett. **14**, 694 (2023).

[15] T. Furukawa, Y. Shimokawa, K. Kobayashi, and T. Itou, Observation of current-induced bulk magnetization in elemental tellurium, Nat. Commun. **8**, 954 (2017).

[16] A. Aronov and Y. B. Lyanda-Geller, Nuclear electric resonance and orientation of carrier spins by an electric field, Sov. J. Exp. Theor. Phys. Lett. **50**, 431 (1989).

[17] V. M. Edelstein, Spin polarization of conduction electrons induced by electric current in two-dimensional asymmetric electron systems, Solid State Commun. **73**, 233 (1990).

[18] E. Rashba, Properties of semiconductors with an extremum loop, Sov. Phys.-Solid State **2**, 1109 (1960).

[19] Y. A. Bychkov and É. I. Rashba, Properties of a 2D electron gas with lifted spectral degeneracy, JETP Lett. **39**, 78 (1984).

[20] Y. A. Bychkov and E. I. Rashba, Oscillatory effects and the magnetic susceptibility of carriers in inversion layers, J. Phys. C **17**, 6039 (1984).

[21] A. Roy, F. T. Cerasoli, A. Jayaraj, K. Tenzin, M. B. Nardelli, and J. Sławińska, Long-range current-induced spin accumulation in chiral crystals, npj Comput. Mater. **8**, 243 (2022).

[22] J. Sławińska, Spin selectivity in elemental tellurium and other chiral materials, Appl. Phys. Lett. **123**, 240504 (2023).

[23] S. Zhang and Z. Yang, Intrinsic spin and orbital angular momentum Hall effect, Phys. Rev. Lett. **94**, 066602 (2005).

[24] B. A. Bernevig, T. L. Hughes, and S.-C. Zhang, Orbitronics: The intrinsic orbital current in *p*-doped silicon, Phys. Rev. Lett. **95**, 066601 (2005).

[25] H. Kontani, T. Tanaka, D. Hirashima, K. Yamada, and J. Inoue, Giant intrinsic spin and orbital Hall effects in Sr_2MO_4 (M = Ru, Rh, Mo), Phys. Rev. Lett. **100**, 096601 (2008).

[26] T. Tanaka, H. Kontani, M. Naito, T. Naito, D. S. Hirashima, K. Yamada, and J. Inoue, Intrinsic spin Hall effect and orbital Hall effect in 4*d* and 5*d* transition metals, Phys. Rev. B **77**, 165117 (2008).

[27] H. Kontani, T. Tanaka, D. Hirashima, K. Yamada, and J. Inoue, Giant orbital Hall effect in transition metals: Origin of large spin and anomalous Hall effects, Phys. Rev. Lett. **102**, 016601 (2009).

[28] D. Go, D. Jo, C. Kim, and H.-W. Lee, Intrinsic spin and orbital Hall effects from orbital texture, Phys. Rev. Lett. **121**, 086602 (2018).

[29] A. Pezo, D. G. Ovalle, and A. Manchon, Orbital Hall effect in crystals: Interatomic versus intra-atomic contributions, Phys. Rev. B **106**, 104414 (2022).

[30] L. M. Canonico, T. P. Cysne, A. Molina-Sanchez, R. Muniz, and T. G. Rappoport, Orbital Hall insulating phase in transition metal dichalcogenide monolayers, Phys. Rev. B **101**, 161409 (2020).

[31] T. P. Cysne, S. Bhowal, G. Vignale, and T. G. Rappoport, Orbital Hall effect in bilayer transition metal dichalcogenides: From the intra-atomic approximation to the Bloch states orbital magnetic moment approach, Phys. Rev. B **105**, 195421 (2022).

[32] L. Salemi and P. M. Oppeneer, Theory of magnetic spin and orbital Hall and Nernst effects in bulk ferromagnets, Phys. Rev. B **106**, 024410 (2022).

[33] O. Busch, I. Mertig, and B. Göbel, Orbital Hall effect and orbital edge states caused by *s* electrons, Phys. Rev. Res. **5**, 043052 (2023).

[34] Y.-G. Choi, D. Jo, K.-H. Ko, D. Go, K.-H. Kim, H. G. Park, C. Kim, B.-C. Min, G.-M. Choi, and H.-W. Lee, Observation of the orbital Hall effect in a light metal Ti, Nature (London) **619**, 52 (2023).

[35] I. Lyalin, S. Alikhah, M. Berritta, P. M. Oppeneer, and R. K. Kawakami, Magneto-optical detection of the orbital Hall effect in chromium, Phys. Rev. Lett. **131**, 156702 (2023).

[36] O. Busch, F. Ziolkowski, B. Göbel, I. Mertig, and J. Henk, Ultrafast orbital Hall effect in metallic nanoribbons, Phys. Rev. Res. **6**, 013208 (2024).

[37] B. Göbel and I. Mertig, Orbital Hall effect accompanying quantum Hall effect: Landau levels cause orbital polarized edge currents, Phys. Rev. Lett. **133**, 146301 (2024).

[38] B. Göbel, L. Schimpf, and I. Mertig, Topological orbital Hall effect caused by skyrmions and antiferromagnetic skyrmions, Commun. Phys. **8**, 17 (2025).

[39] L. Levitov, Y. V. Nazarov, and G. Eliashberg, Magnetoelectric effects in conductors with mirror isomer symmetry, Sov. J. Exp. Theor. Phys. **61**, 133 (1985).

[40] T. Yoda, T. Yokoyama, and S. Murakami, Current-induced orbital and spin magnetizations in crystals with helical structure, Sci. Rep. **5**, 12024 (2015).

[41] T. Yoda, T. Yokoyama, and S. Murakami, Orbital Edelstein effect as a condensed-matter analog of solenoids, Nano Lett. **18**, 916 (2018).

[42] D. Go, J.-P. Hanke, P. M. Buhl, F. Freimuth, G. Bihlmayer, H.-W. Lee, Y. Mokrousov, and S. Blügel, Toward surface orbitronics: Giant orbital magnetism from the orbital Rashba effect at the surface of *sp*-metals, Sci. Rep. **7**, 46742 (2017).

[43] L. Salemi, M. Berritta, A. K. Nandy, and P. M. Oppeneer, Orbitally dominated Rashba-Edelstein effect in noncentrosymmetric antiferromagnets, Nat. Commun. **10**, 5381 (2019).

[44] A. Johansson, B. Göbel, J. Henk, M. Bibes, and I. Mertig, Spin and orbital Edelstein effects in a two-dimensional electron gas: Theory and application to $SrTiO_3$ interfaces, Phys. Rev. Res. **3**, 013275 (2021).

[45] Y. Liu, J. Xiao, J. Koo, and B. Yan, Chirality-driven topological electronic structure of DNA-like materials, Nat. Mater. **20**, 638 (2021).

[46] B. Kim, D. Shin, S. Namgung, N. Park, K.-W. Kim, and J. Kim, Optoelectronic manifestation of orbital angular momentum driven by chiral hopping in helical Se chains, ACS Nano **17**, 18873 (2023).

[47] A. El Hamdi, J.-Y. Chauleau, M. Boselli, C. Thibault, C. Gorini, A. Smogunov, C. Barreteau, S. Gariglio, J.-M. Triscone, and M. Viret, Observation of the orbital inverse Rashba–Edelstein effect, Nat. Phys. **19**, 1855 (2023).

[48] S. Leiva-Montecinos, J. Henk, I. Mertig, and A. Johansson, Spin and orbital Edelstein effect in a bilayer system with Rashba interaction, Phys. Rev. Res. **5**, 043294 (2023).

[49] K. Hagiwara, Y.-J. Chen, D. Go, X. L. Tan, S. Grytsiuk, K.-H. O. Yang, G.-J. Shu, J. Chien, Y.-H. Shen, X.-L. Huang *et al.*, Orbital topology of chiral crystals for orbitronics, Adv. Mater. **37** 2418040 (2025).

[50] A. Johansson, Theory of spin and orbital Edelstein effects, J. Phys.: Condens. Matter **36**, 423002 (2024).

[51] J. M. Lee, M. J. Park, and H.-W. Lee, Orbital Edelstein effect of electronic itinerant orbital motion at edges, Phys. Rev. B **110**, 134436 (2024).

[52] M.-C. Chang and Q. Niu, Berry phase, hyperorbits, and the Hofstadter spectrum: Semiclassical dynamics in magnetic Bloch bands, Phys. Rev. B **53**, 7010 (1996).

[53] D. Xiao, J. Shi, and Q. Niu, Berry phase correction to electron density of states in solids, Phys. Rev. Lett. **95**, 137204 (2005).

[54] T. Thonhauser, D. Ceresoli, D. Vanderbilt, and R. Resta, Orbital magnetization in periodic insulators, Phys. Rev. Lett. **95**, 137205 (2005).

[55] D. Ceresoli, T. Thonhauser, D. Vanderbilt, and R. Resta, Orbital magnetization in crystalline solids: Multi-band insulators, Chern insulators, and metals, Phys. Rev. B **74**, 024408 (2006).

[56] A. Raoux, F. Piéchon, J.-N. Fuchs, and G. Montambaux, Orbital magnetism in coupled-bands models, Phys. Rev. B **91**, 085120 (2015).

[57] B. Göbel, A. Mook, J. Henk, and I. Mertig, Magnetoelectric effect and orbital magnetization in skyrmion crystals: Detection and characterization of skyrmions, Phys. Rev. B **99**, 060406 (2019).

[58] F. D. M. Haldane, Model for a quantum Hall effect without Landau levels: Condensed-matter realization of the "parity anomaly", Phys. Rev. Lett. **61**, 2015 (1988).

[59] Note that increasing the helix period c would lead to a decreased hopping amplitude t.

[60] J. Li, A. Ciani, J. Gayles, D. Papaconstantopoulos, N. Kioussis, C. Grein, and F. Aqariden, Non-orthogonal tight-binding model for tellurium and selenium, Philos. Mag. **93**, 3216 (2013).

[61] C. L. Kane and E. J. Mele, Z_2 topological order and the quantum spin Hall effect, Phys. Rev. Lett. **95**, 146802 (2005).

[62] B. Göbel, I. Mertig, and S. Lounis, Chirality-induced selectivity of angular momentum by orbital Edelstein effect in carbon nanotubes, arXiv:2504.07665.

[63] D. Jo, D. Go, G.-M. Choi, and H.-W. Lee, Spintronics meets orbitronics: Emergence of orbital angular momentum in solids, npj Spintronics **2**, 19 (2024).

[64] D. Lee, D. Go, H.-J. Park, W. Jeong, H.-W. Ko, D. Yun, D. Jo, S. Lee, G. Go, J. H. Oh *et al.*, Orbital torque in magnetic bilayers, Nat. Commun. **12**, 6710 (2021).

[65] G. Sala, H. Wang, W. Legrand, and P. Gambardella, Orbital Hanle magnetoresistance in a 3D transition metal, Phys. Rev. Lett. **131**, 156703 (2023).

[66] Data are provided for Figs. 6 and 7. All other results were calculated analytically, https://doi.org/10.5281/zenodo.16690046.

[67] Z.-G. Yu, Chirality-induced spin–orbit coupling, spin transport, and natural optical activity in hybrid organic–inorganic perovskites, J. Phys. Chem. Lett. **11**, 8638 (2020).

[68] G. Dresselhaus, Spin-orbit coupling effects in zinc blende structures, Phys. Rev. **100**, 580 (1955).